International Journal of Heat and Mass Transfer 268 (2026) 129024

Contents lists available at ScienceDirect

International Journal of Heat and Mass Transfer

journal homepage: www.elsevier.com/locate/ijhmt

Non-straight boundary regulates natural convection pattern in porous media

Yumin Wang [a,*], Jiansong Wu [a], Ke Xu [b,*]

[a] School of Emergency Management and Safety Engineering, China University of Mining & Technology, Beijing 100083, China
[b] Department of Energy and Resources Engineering, College of Engineering, Peking University, Beijing 100871, China

ARTICLE INFO

Keywords:
Porous media
Non-Straight boundary
Rayleigh–Darcy convection
Pattern formation
Heat transfer efficiency

ABSTRACT

Natural convection in porous media is commonly studied with flat boundaries, whereas realistic geological and engineering interfaces are often non-straight. Here we perform transient two-dimensional numerical simulations based on the Brinkman equations coupled with heat transfer in porous media to investigate Rayleigh-Darcy convection over sinusoidal non-straight bottom boundaries in a porous layer of width $L = 120$ mm and mean height $h = 20$ mm. The simulations cover $Ra = 1\text{–}3 \times 10^5$ at porosity $\varphi = 0.42$, with boundary geometries $n = 9$, 15, and 30 and amplitudes $e = 2$ and 5 mm, and compare the results with the straight-boundary case. Heat-transfer efficiency is evaluated by Nu/Ra. Relative to the classical straight-boundary case, a clear crossover is observed. For $Ra < 1300$, the non-straight boundary triggers localized convection in the troughs and increases the effective convective height, enhancing Nu/Ra by up to 2.43 times. For $Ra > 1300$, the troughs become weakly ventilated and evolve into stagnant dead zones; the main circulation bypasses these regions, producing a stagnant-trough-induced thermal short-circuit and lowering the effective convective height. Consequently, in the representative $n = 15$, $e = 5$ mm case, the non-straight boundary suppresses heat transfer and reduces Nu/Ra by about 32% at $Ra = 3 \times 10^5$. These results show that non-straight boundaries induce a regime-dependent transition from transport enhancement to transport suppression in porous convection.

1. Introduction

Natural convection in fluid-saturated porous media controls heat and mass transfer in a wide range of natural and engineered systems, including geothermal energy recovery, underground carbon storage, hydrothermal circulation, and thawing or freezing fronts [1–4]. In its canonical form, this process is commonly studied as Horton-Rogers-Lapwood convection, the porous-medium analogue of Rayleigh-Benard convection, in which a porous layer is heated from below and cooled from above [5,6]. Two dimensionless quantities are central to this problem: the Rayleigh-Darcy number, *Ra*, which measures the competition between buoyancy and diffusive-viscous resistance, and the Nusselt number, *Nu*, which quantifies the enhancement of total heat flux relative to pure conduction [3].

For flat, parallel boundaries, the major flow and transport regimes are now relatively well established. Linear stability theory predicts the onset of convection at a critical Rayleigh-Darcy number close to $4\pi^2$ [5, 6], while experiments and simulations have clarified how plume organization and heat-transfer efficiency evolve as *Ra* increases [7–9].

Recent studies at high *Ra* have further shown that heat transport in porous media is controlled by thin boundary layers, plume interactions, and multiscale flow organization, leading to modern scaling descriptions that connect Rayleigh-Darcy convection with Grossmann-Lohse-type ideas and the approach to strong-convection regimes [10–12]. Despite this substantial progress, however, the overwhelming majority of theoretical, numerical, and experimental studies still adopt a highly idealized geometry with planar horizontal boundaries.

That simplification is convenient, but it is not always representative of realistic porous systems. In geological and engineering settings, the interfaces that bound a porous layer are often non-straight because of sedimentation, erosion, dissolution, fracture roughness, or phase-change-induced topography. Such geometric irregularities can reorganize local flow pathways, alter boundary-layer development, and change the spatial distribution of transport-active regions. Recent pore-scale studies have shown that convective heat transfer in porous media can depend strongly on structural details and local geometry rather than on *Ra* alone [13–15].

In related rough- or wavy-boundary configurations, substantial

* Corresponding authors.
E-mail addresses: b202508@cumtb.edu.cn (Y. Wang), kexu1989@pku.edu.cn (K. Xu).

https://doi.org/10.1016/j.ijheatmasstransfer.2026.129024
Received 15 January 2026; Received in revised form 5 May 2026; Accepted 16 May 2026
Available online 26 May 2026

geometry-induced changes in circulation patterns and transport behavior have also been reported for Brinkman-Benard systems, porous cavities, sinusoidally heated porous media, and rough fractures [16–20]. These studies make clear that boundary geometry matters, but they do not yet resolve a key question for canonical Rayleigh-Darcy convection: when a horizontally periodic porous layer is heated from a sinusoidal bottom boundary, does the non-straight geometry systematically enhance heat transfer, or can it suppress transport once convection becomes vigorous?

This question is nontrivial because the influence of boundary geometry need not be monotonic. At low Ra, a non-straight boundary may increase the effective transfer area and trigger localized circulation in trough regions that would remain inactive for a flat boundary. At high Ra, however, the same geometry may create sheltered trough regions with weak fluid exchange, so that part of the domain becomes partially decoupled from the global circulation. In that case, boundary roughness could promote transport in one regime but hinder it in another. What is still lacking is a unified physical picture that link$_s$ non-straight boundary geometry to regime-dependent heat-transfer behavior across the full transition from diffusion-dominated to vigorous convection in Rayleigh-Darcy systems.

In this study, we address this gap using high-resolution two-dimensional numerical simulations of Rayleigh-Darcy convection over sinusoidal non-straight bottom boundaries across a broad range of $Ra = 1–3 \times 10^5$. The results reveal a clear crossover in heat-transfer efficiency: compared with the classical straight-boundary case, the non-straight boundary enhances Nu/Ra in the diffusion-dominated and transitional regimes, but suppresses Nu/Ra once Ra becomes sufficiently large. We show that the low-Ra enhancement is associated with localized convection and an enlarged effective convective height, whereas the high-Ra suppression arises from stagnant trough regions that form transport-inactive dead zones. These stagnant pockets force the main circulation to bypass the troughs, producing a thermal short-circuit and reducing the effective height available for active convection. By combining flow visualization, density-field analysis, heat-flux statistics, and scaling arguments, we establish a unified mechanism for the transition from enhancement to suppression and show that this behavior is robust across different boundary amplitudes and wavelengths. The results provide a clearer physical basis for understanding how non-straight boundaries regulate heat transport in porous media and offer new insight into convection over rough geological interfaces.

2. Materials and methods

Fig. 2(a) shows the physical domain considered in this study. We model one laterally periodic two-dimensional unit cell of a fluid-saturated porous layer with width $L = 120$ mm and mean height $h = 20$ mm. The lower boundary is sinusoidal and the upper boundary is flat, so the setup represents an infinitely extended repeating geometry rather than a laterally confined enclosure.

The pore space is occupied by a single-phase Newtonian fluid, and the thermophysical and porous-medium parameters used in the present simulations were adopted from our previously published experimentally characterized system [21]. In that experimental system, mono-dispersed spherical glass beads were packed as the porous medium, and the porosity was measured by a liquid-level displacement method. Specifically, the beads were first packed in a container with a constant cross-sectional area to form a porous layer of height H_2. Water was then added to fill the pore space, and the liquid-level change corresponding to the water volume entering the pore space was recorded as an equivalent height H_1 in the same container. Because the cross-sectional area is identical for both measurements, the ratio of the pore volume to the bulk packed-bed volume can be written as $\varphi = H_1/H_2$. The measured porosity for different bead diameters ranged from 0.408 to 0.455, and the average value $\varphi = 0.42$ was therefore adopted in the present numerical simulations. The solid phase is not resolved as individual particles; instead, it is represented as a rigid, homogeneous, isotropic porous matrix characterized by porosity, permeability, effective thermal conductivity, and effective volumetric heat capacity. The present work itself is purely numerical and does not report new experiments. The sinusoidal bottom boundary is defined by $y_b(x) = e \cos(2\pi n x/L)$, where e is the amplitude and n is the number of waves within one horizontal period.

2.1. Governing equations and boundary conditions

This section presents the dimensional governing equations, boundary conditions, and initial conditions. The nondimensional equations, boundary conditions, and dimensionless groups are then provided in Section 2.2 to define the controlling parameters used in the simulations.

Dimensional Fluid Flow Model. The fluid is treated as incompressible except in the buoyancy term, and the flow is solved in time-dependent form using the transient Brinkman equation [3,22]. While classical Darcy's law is sufficient for bulk porous flows, it neglects viscous shear stresses that become important near solid boundaries. In the present study, the non-straight bottom geometry induces strong near-wall shear and requires a no-slip condition at the undulating interface; therefore, the Brinkman viscous term is retained. Under the Boussinesq approximation and the Stokes-flow assumption, the governing equations for continuity and momentum are written as:

$$\nabla\cdot\mathbf{u} = 0 \tag{1a}$$

$$\frac{\rho_0}{\varphi}\frac{\partial\mathbf{u}}{\partial t} = -\nabla p + \nabla\cdot\left(\frac{\mu_{\text{eff}}}{\varphi}\nabla\mathbf{u}\right) - \frac{\mu}{k}\mathbf{u} + \rho\mathbf{g} \tag{1b}$$

where u is the Darcy velocity vector, p is the pressure, φ is the porosity, and k is the permeability of the porous medium. μ denotes the dynamic viscosity of the fluid, and μ_{eff} represents the effective viscosity, which is typically taken as μ for fluid-saturated porous media. The term ρg represents the gravitational body force.

Equation of State. To close the system, the fluid density ρ is assumed to depend linearly on temperature according to the Boussinesq approximation. This formulation couples the flow field with the temperature field:

$$\rho = \rho_0[1 - \beta(T - T_c)] \tag{2}$$

where ρ_0 is the reference fluid density at the reference temperature T_c, and β is the thermal expansion coefficient. This constitutive relation ensures that density variations drive the natural convection via the buoyancy term in Eq. (1b).

Heat Transfer Model. The transient heat transport in the fluid-saturated porous medium is modeled under local thermal equilibrium between the fluid and the solid matrix [3,23]:

$$(\rho C_p)_{\text{eff}}\frac{\partial T}{\partial t} + (\rho C_p)_f\mathbf{u}\cdot\nabla T = \nabla\cdot(k_{\text{eff}}\nabla T) \tag{3}$$

where T is the temperature. $(\rho C_p)_f$ is the volumetric heat capacity of the fluid. $(\rho C_p)_{eff}$ and k_{eff} are the effective volumetric heat capacity and effective thermal conductivity of the saturated porous medium, respectively, defined as:

$$(\rho C_p)_{\text{eff}} = \varphi(\rho C_p)_f + (1-\varphi)(\rho C_p)_s \tag{4}$$

$$k_{\text{eff}} = \varphi k_f + (1-\varphi)k_s \tag{5}$$

Here, subscripts f and s denote the fluid and solid phases, respectively. The first term in Eq. (3) represents transient heat storage, the second term describes convective heat transport, and the term on the right-hand side accounts for thermal conduction.

The computational domain represents one periodic unit cell with width $L = 120$ mm and average height $h = 20$ mm. Because the boundary geometry repeats horizontally and the objective is to represent a laterally infinite porous layer rather than a sidewall-confined enclosure, periodic boundary conditions are imposed on the vertical sidewalls ($x = 0$ and $x = L$) for both the flow and temperature fields. In dimensional form, the lateral periodic conditions are $u(0,y,t) = u(L,y,t)$ and $T(0,y,t) = T(L,y,t)$.

$$\mathbf{u}(0,y) = \mathbf{u}(L,y), \quad T(0,y) = T(L,y) \tag{6}$$

Bottom Boundary. The bottom boundary is rigid and non-straight, characterized by a sinusoidal profile defined as $y_b(x) = e\cos(2\pi\, n\, x/L)$, where e is the amplitude and n is the wavenumber describing the number of waves within the domain width L. This boundary is maintained at a constant high temperature T_d. Because the bottom is a solid wall in the Brinkman model, a no-slip condition is applied, i.e., $u = 0$ and $T = T_d$ at $y = y_b(x)$.

$$\mathbf{u} = 0, T = T_d, \text{ at } y = y_b(x) \tag{7}$$

Top Boundary. The top boundary is treated as an open boundary for the flow field, rather than as a rigid impermeable wall. This open boundary allows the pressure/normal-flow adjustment required by the present vertically driven open-top configuration, while the thermal reference at the top is associated with the cold/open-boundary temperature T_u ($T_u < T_d$). In the dimensional boundary-condition statement, this is written as an open-flow condition at $y = h$ together with the corresponding cold thermal condition $T = T_u$ used to define the imposed temperature difference $\Delta T = T_d$ - T_u.

$$T = T_u, \text{ at } y = h \tag{8}$$

Initial Conditions. The simulation starts from a static state with a uniform temperature field equal to the cold wall temperature T_u. A small random perturbation is superimposed on the initial temperature field to trigger the onset of convection:

$$\mathbf{u} = 0, T(x,y,0) = T_u + \delta T(x,y) \tag{9}$$

where δT denotes a random perturbation with a magnitude of $10^{-3}\, T_u$. Since the lower boundary is hotter than the upper boundary and the fluid density decreases with temperature under the Boussinesq approximation ($\rho_d < \rho_u$), the initial conductive state is gravitationally unstable and evolves naturally into buoyancy-driven convection.

2.2. Nondimensional governing equations and dimensionless groups

To facilitate a general analysis independent of specific fluid properties, the dimensional governing equations and boundary conditions above are nondimensionalized using the porous-layer height h as the characteristic length, the thermal-diffusion velocity α_f/h as the characteristic velocity, the thermal-diffusion time h^2/α_f as the characteristic time, the pressure scale $\mu\alpha_f/k$, and the temperature difference $\Delta T = T_d$ - T_u as the characteristic temperature scale. The corresponding dimensionless variables are:

$$X = \frac{x}{h}, Y = \frac{y}{h}, \tau = \frac{\alpha_f t}{h^2}, \mathbf{U} = \frac{\mathbf{u}h}{\alpha_f}, P = \frac{kp}{\mu\alpha_f}, \theta = \frac{T - T_u}{\Delta T} \tag{10}$$

With these definitions, the nondimensional continuity, momentum, and energy equations are given, respectively, by:

$$\nabla^* \cdot \mathbf{U} = 0 \tag{11}$$

$$\frac{Da}{\varepsilon_p \mathrm{Pr}}\frac{\partial \mathbf{U}}{\partial \tau} = -\nabla^* P + Da\nabla^{*2}\mathbf{U} - \mathbf{U} + Ra\theta\mathbf{e}_y \tag{12}$$

$$\sigma\frac{\partial\theta}{\partial\tau} + \mathbf{U}\cdot\nabla^*\theta = \lambda\nabla^{*2}\theta \tag{13}$$

$Pr = \nu/\alpha_f$, $\sigma = (\rho C_p)_{eff}/(\rho C_p)_f$, $\lambda = k_{eff}/k_f$, and $Da = k/h^2$. Here Da is fixed by the permeability and height scale and is not varied as an independent control parameter. The corresponding dimensionless boundary conditions are as follows. The side boundaries are periodic for both velocity and temperature. The bottom wall satisfies $U = 0$ and $\theta = 1$ at $Y = y_b/h$. The top boundary is an open-flow boundary with $\theta = 0$ used as the cold thermal reference. These conditions correspond directly to the dimensional boundary conditions listed above. The convective flow behavior is primarily controlled by the Rayleigh-Darcy number (Ra), which characterizes the ratio of the destabilizing buoyancy force to the stabilizing viscous and diffusive effects:

$$Ra = \frac{g\beta\Delta T k h}{\nu\alpha_f} \tag{14}$$

where g is the gravitational acceleration, β is the thermal expansion coefficient, k is the permeability, ν is the kinematic viscosity ($\nu = \mu/\rho_0$), and α_f is the thermal diffusivity of the fluid. In this study, numerical simulations are performed over a wide range of Ra from 1 to 3×10^5 to capture the transition from conduction-dominated to convection-dominated regimes.

The permeability and porosity are fixed throughout the present simulations, and the porosity is set to $\varphi = 0.42$. This configuration keeps the flow in the Darcy-dominated regime in the bulk porous medium, while the Brinkman viscous term is retained to satisfy the no-slip condition at the fluid-solid interfaces. Together with the very small porous Reynolds number discussed below, this indicates that all simulated cases remain in a laminar, creeping-flow porous-convection regime. Inertial non-Darcy corrections such as Forchheimer-type resistance can become important in higher-velocity porous-flow applications (Xue et al., 2025; Yadav et al., 2016), but they were not activated in the present low-Re simulations.

Furthermore, to verify that inertial effects remain negligible, we estimate a permeability-based porous Reynolds number, rather than a channel-flow Reynolds number, following standard porous-medium scaling [3,23]:

$$\mathrm{Re} = \frac{u\sqrt{k}}{\nu} \tag{15}$$

where $\sqrt{k}$ is the intrinsic porous length scale of the porous medium, ν is the kinematic viscosity, and u denotes the characteristic Darcy velocity defined above. In the present manuscript, Re is used only as an a posteriori indicator of inertial effects and does not rely on a particle-diameter input.

Throughout all simulations in this study, the estimated Reynolds number remains much smaller than unity ($Re << 1$). This confirms that inertial effects are negligible, that the flow remains in the laminar creeping-flow regime, and that neglecting both the nonlinear convective term $(u\cdot\nabla)u$ and the Forchheimer correction in the governing momentum equation is justified.

2.3. Numerical Implementation and Verification

The governing equations are solved using the finite element method (FEM) implemented in COMSOL Multiphysics. We utilize quadratic Lagrange elements for the velocity field and linear elements for the pressure and temperature fields to ensure numerical stability and accuracy.

The numerical simulation cases used in this study are summarized in Table 1. Each simulation group (Sim.#) was conducted for Ra = 1, 10, 60, 100, 300, 500, 1000, 3000, 5000, 10 000, 20 000, and 300 000,

Table 1
Geometry parameters of the simulated cases.

Sim. #	Sim. 1	Sim. 2	Sim. 3	Sim. 4	Sim. 5	Sim. 6	Sim. 7
n	0	9	9	15	15	30	30
$\lambda = L/n$, (mm)	0	13.3	13.3	8	8	4	4
e (mm)	0	2	5	2	5	2	5

resulting in a total of $7 \times 12 = 84$ valid simulation datasets.

Grid Independence Test. To assess mesh sensitivity, the regular grid used for the production simulations was compared with a refined grid for the representative geometry $n = 15$ and $e = 5$ mm over $Ra = 1000$, 10 000, 20 000, and 300 000. All other model settings were kept identical to those used in the production simulations. The case $Ra = 1000$ was first selected because it lies close to the transitional range discussed in the Results section, and the additional larger-Ra cases were included to address mesh sensitivity under stronger convection, including the highest simulated Rayleigh-Darcy number. As shown in Table 2, Nu_{g1} denotes the heat-transfer result obtained using the regular grid, whereas Nu_{g2} denotes the result obtained using a refined grid. The two-dimensional computational mesh used for the production simulations is provided in Supplementary Fig. S1. The relative differences remain within 5%, indicating that the grid resolution is adequate for the present parametric study.

Time-Step Independence Test. A time-step independence test was performed for the same representative geometry and fixed model settings, as shown in Table 3. In the production simulations, the solver time stepping was set to automatic, with the solution output controlled by a range setting with a 10 s interval. To verify that this automatic setting is sufficiently accurate, an additional calculation was performed with the maximum time step restricted to 1 s. Here, Nu_{s1} denotes the 1 s maximum-time-step result and Nu_{s2} denotes the automatic-time-step result. The relative differences remain small, confirming that the automatic time-step setting is sufficient. Considering the convergence behavior and the computational cost of the 84-case simulation campaign, the regular-grid and automatic-time-step settings were used for the production runs.

Validation. The numerical solver was first assessed for the flat-boundary case ($e = 0$) by comparison with the benchmark *Nu-Ra* scaling reported by Zhu et al. [10], as shown in Fig. 1. A one-to-one experimental dataset for the present periodic non-straight geometry is not available, so we do not claim direct experimental validation of the exact configuration studied here. Instead, the thermophysical and porous-medium parameters were adopted from our previously published experimentally characterized system [21], and the benchmark comparison, together with the grid- and time-step-independence tests above, supports the reliability of the numerical method. In addition, the present temperature field is qualitatively compared with the high-Rayleigh-number Rayleigh-Darcy convection temperature field reported by Hewitt et al. [24] in Supplementary Fig. S2. Because the benchmark and present domains have different aspect ratios, the lower 2/9-height region of the Hewitt et al. field is enlarged for comparison; this region shows highly similar near-bottom proto-plume structures to the present $Ra = 20$ 000 straight-boundary result. The spatiotemporal evolution of the convective structures shown in Supplementary Fig. S3 is likewise consistent with canonical porous-convection behavior [10,11,24].

To elucidate the fundamental mechanisms governing the heat transfer and flow dynamics, we selected the case with $n = 15$ and $e = 5$ mm as the representative configuration for the detailed analysis in the main text. This case was selected after comparison with the full simulation dataset because it provides the clearest diagnostic example of the transition from low-Ra enhancement to high-Ra suppression relative to the straight-boundary baseline. Accordingly, the main-text mechanistic figures focus on this representative non-straight geometry. The other geometries, including the $n = 30$ cases, are not omitted; they are included in the full 84-case dataset and are used in Supplementary Material Section S5 to show how the crossover strength depends on wavenumber and amplitude.

Table 2
Grid-independence test for the representative case ($n = 15$, $e = 5$ mm; $\varphi = 0.42$) at different Rayleigh-Darcy numbers.

Ra	Nu_{g1}	Nu_{g2}	Relative error
1000	4.423596264	4.313796042	2.55%
10 000	17.11556284	16.53008621	3.54%
20 000	31.8575533	30.47031551	4.55%
300 000	515.8633913	491.5150237	4.95%

Table 3
Time-step independence test for the representative case ($n = 15$, $e = 5$ mm; $\varphi = 0.42$), comparing the 1 s maximum-time-step setting with the automatic time-step setting.

Ra	Nu_{s1}	Nu_{s2}	Relative error
1000	4.29	4.38	2.19%
3000	7.50	7.82	4.31%
5000	10.00	10.32	3.18%
10 000	17.18	17.08	0.56%
20 000	30.47	30.73	0.85%
300 000	468.37	477.97	2.05%

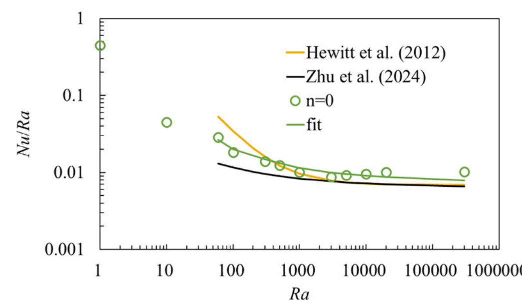

Fig. 1. Quantitative validation of the flat-boundary case: variation of the convection heat transfer efficiency (*Nu/Ra*) with *Ra* under straight boundary conditions. The black line represents the results from Zhu et al. [10], the green circles denote the numerical simulation data points obtained in this study, and the green line corresponds to the curve fitted according to Eq. (S2).

Heat Transfer Quantification. The global heat-transfer efficiency is quantified by the Nusselt number (*Nu*). In the present work, Eq. (16) is defined from the vertical component of the total heat flux across one horizontal period. Therefore, the conductive term uses the vertical temperature gradient $\partial T/\partial y$ rather than the local boundary-normal derivative along the sinusoidal wall. The line integral follows the non-straight bottom boundary, whereas the normalization uses the projected width L so that the non-straight and straight cases can be compared on the same global basis [3]:

$$Nu = \frac{1}{L}\int_0^L \left(-\frac{\partial T}{\partial y} + vT\right)_{y=y_b} \frac{dx}{\Delta T/h} \tag{16}$$

where the integration path follows the non-straight bottom profile $y_b(x)$, but the integrand represents the vertical heat-flux contribution crossing the porous layer. This definition is adopted because the quantity of interest in Rayleigh-Darcy convection is the net vertical heat transport between the bottom and top boundaries. For the flat boundary case ($e = 0$), Eq. (16) reduces to the standard expression in Eq. (17), where angle brackets denote horizontal averaging.

$$Nu = -\left\langle \frac{\partial T}{\partial y} \right\rangle \Big|_{y=0} \tag{17}$$

3. Results and discussion

3.1. Convection modes and statistical steady state

In the following section, the effects of boundary geometry on heat transfer are examined using the representative case with a wavenumber of $n = 15$ (within one periodic domain) and a wave amplitude of $e = 5$ mm. This case is used because the full dataset shows that it provides the clearest enhancement-to-suppression crossover relative to the straight-boundary baseline, making it the most suitable configuration for discussing the governing mechanism. Unless otherwise stated, the main-text figures show this representative non-straight configuration. The corresponding results for the other simulated geometries, including $n = 30$, are compiled in Supplementary Material Section S5.

Convection Modes. (1) Low Ra conditions (for example, $Ra = 1$). As shown in Fig. 2(b), convection is present but remains weak. The finger structures are stable and primarily constrained by the non-straight boundary geometry. The dynamical evolution is slow: the fingers exhibit almost no lateral motion or merging and eventually reach a stable, stratified configuration. Classical studies by Horton and Rogers [5] and Lapwood [6] indicate that no convection occurs when Ra is less than $4\pi^2$, and heat transfer is purely diffusion-controlled. In contrast, under non-straight bottom boundary conditions, even when Ra is less than $4\pi^2$, the boundary geometry can trigger localized convection near the interface.

(2) Moderate Ra conditions (for example, $Ra = 100$ and 1000). In Fig. 2(b), the influence of convection becomes more pronounced, although mixing remains relatively weak and the density field near the bottom boundary still shows strong stratification. The finger structures begin to merge and drift laterally (see Fig. S3 in the Supplementary Materials for details), entering a more dynamic and complex evolutionary regime. In the statistically steady state, the number of observable fingers decreases, accompanied by frequent merging and morphological reorganization. The finger shapes gradually evolve from sinusoidal patterns to flame-like forms, reflecting enhanced convective mixing and stronger nonlinear interactions [25].

(3) High Ra conditions (for example, $Ra = 3000$, 20 000, and 300 000). As shown in Fig. 2(b), convection becomes strongly intensified, while the density field near the bottom boundary becomes more homogenized. The vigorous convection accelerates the evolution of fingers: they develop a narrow base and a broader upper region, forming wider but fewer plumes. This indicates that, at high Ra, the density-field dynamics become increasingly intense and merger-dominated, leading to the formation of large-scale convective structures. At the highest simulated Rayleigh-Darcy number, $Ra = 300\ 000$, the trough region becomes only weakly ventilated, the main circulation bypasses the troughs more completely, and the suppressive effect of the non-straight boundary on heat-transfer efficiency becomes especially clear. This behavior is consistent with the observations reported by Wang et al. [21].

Statistical Steady State. Probes were placed at the top and bottom boundaries to monitor the vertical heat flux. Fig. 2(c) shows the temporal evolution of the heat flux at the upper and lower boundaries for representative low- and high-Ra cases. The flux values in Fig. 2(c) are nondimensionalized by the time-averaged flux during the statistically steady state. As transport proceeds, the fluxes at both boundaries approach approximately constant mean values, which is used as an indicator that a statistically steady state has been attained. Specifically, when the time-averaged heat flux remains effectively unchanged over a prescribed time interval, the system is deemed to be in a statistically steady state, and the corresponding averaging window is used for the statistical analysis. This criterion is used throughout this study to identify the statistically steady stage in all numerical simulations.

3.2. Convective heat-transfer efficiency Nu/Ra

From Fig. 3, three distinct regimes can be identified. (1) In Regime I ($Ra < 4\pi^2$), the convective heat-transfer efficiency Nu/Ra for the non-straight-bottom configuration is higher than that for the straight-bottom configuration. (2) In Regime II ($4\pi^2 < Ra < 1300$), Nu/Ra decreases with increasing Ra, but the rate of decrease is lower for the non-straight-bottom configuration, so Nu/Ra remains higher than that for the straight-bottom configuration. (3) In Regime III ($Ra > 1300$), Nu/Ra continues to decrease as Ra increases; however, the rate of decrease becomes larger for the non-straight-bottom configuration, and consequently Nu/Ra becomes lower than that for the straight-bottom configuration.

The velocity fields in Fig. 4(a)-(d) correspond to Regime I in Fig. 3. No convection develops in the straight-bottom configuration, whereas clear convective motion occurs in the non-straight-bottom configuration, consistent with our previous work [21]. When Ra is smaller than $4\pi^2$, heat transfer is dominated by diffusion in the straight-bottom

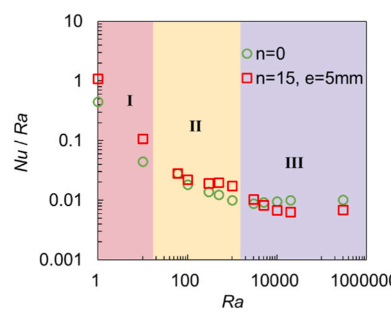

Fig. 3. Heat-transfer efficiency Nu/Ra for the straight boundary and for the representative non-straight boundary ($n = 15$, $e = 5$ mm). The $n = 15$, $e = 5$ mm case is selected here because it provides the clearest enhancement-to-suppression crossover in the full dataset. Green circles: straight boundary. Red squares: non-straight boundary. Regimes I-III follow the classical straight-boundary classification. Results for the other non-straight geometries, including $n = 30$, are provided in Supplementary Material Section S5.

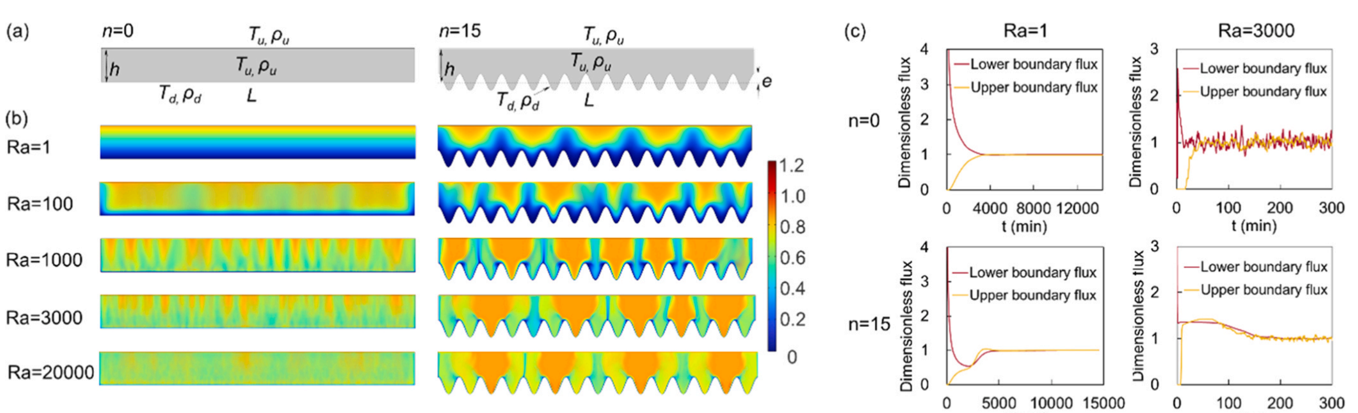

Fig. 2. Boundary geometry, statistically steady density fields, and normalized boundary heat fluxes. (a) Straight and non-straight bottom boundaries. (b) Time-averaged dimensionless density fields at statistical steady state. (c) Boundary heat fluxes, each normalized by its own temporal mean in the statistical steady state.

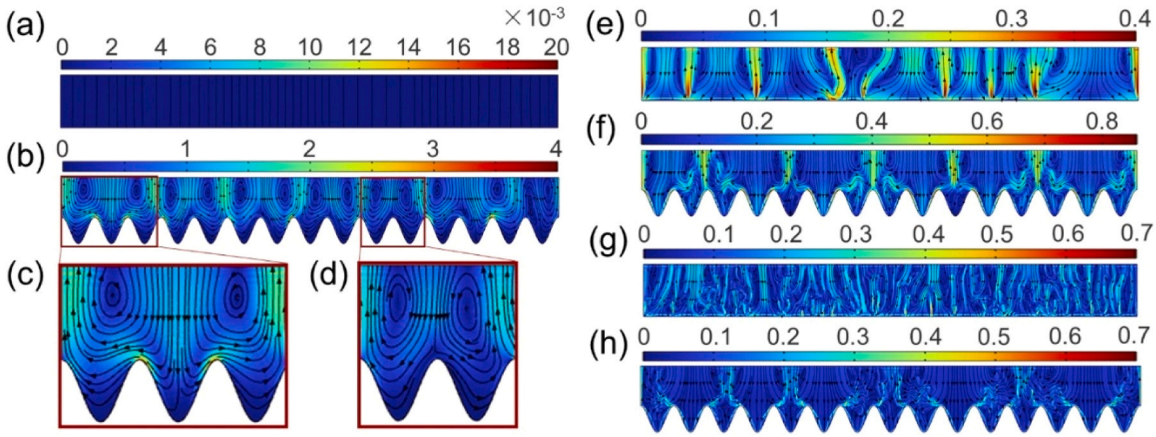

Fig. 4. Velocity fields normalized by the Darcy velocity scale u. (a,b) Straight and non-straight boundaries in Regime I. (c,d) Enlarged local views from panel (b), highlighting two distinct trough-flow patterns. (e,f) Straight and non-straight boundaries in Regime II. (g,h) Straight and non-straight boundaries in Regime III.

configuration. However, the non-straight bottom boundary induces local convection, which leads to a larger value of Nu/Ra than that of the straight-bottom configuration, as shown in Regime I of Fig. 3.

In addition, Fig. 4 reveals more detailed flow features that were not emphasized in our previous work [21]. In Wang et al. [21], the local convection near the non-straight bottom boundary is similar to that shown in Fig. 4(c). Here, however, we identify two distinct flow patterns near the non-straight bottom. In Fig. 4(c), the flow descends into the trough and then moves toward the crest. This occurs because the perpendicular bisector of the line joining the two vortices intersects the non-straight bottom boundary at a trough. In Fig. 4(d), by contrast, the flow still descends into the trough but then moves sideways along the bottom. This is because the perpendicular bisector of the line joining the two vortices intersects the non-straight bottom boundary at a crest.

The velocity fields in Fig. 4(e)–(f) correspond to regime II in Fig. 3. In this regime, the effective heat-transfer height h of the flow in the non-straight-bottom configuration is larger than that in the straight-bottom configuration (this trend is also evident in Fig. 7). The velocity fields in Fig. 4(g)–(h) correspond to regime III in Fig. 3. In this case, the effective penetration height H in the non-straight-bottom configuration becomes smaller than that in the straight-bottom configuration (again consistent with Fig. 7). Based on the above reasons, the heat-transfer efficiency in the non-straight-bottom configuration is higher than that in the straight-bottom configuration in regimes I and II, but lower in regime III.

3.3. Convective characteristics

As shown in Fig. 5(a), three distinct regimes can be identified based on the Rayleigh-Darcy number. The root-mean-square velocity is calculated over the statistically steady averaging window as $u_{rms} = \left[\frac{1}{t_2 - t_1}\int_{t_1}^{t_2} \langle |u(x,y,t)|^2 \rangle_{\Omega} dt\right]^{1/2}$, where $|u|$ is the magnitude of the Darcy velocity, $\langle\cdot\rangle_{\Omega}$ denotes spatial averaging over the computational domain, and t_1 and t_2 are the start and end times of the statistically steady averaging window. First, in the low-Rayleigh-number regime ($Ra = 1$–300), the root-mean-square velocity ratio between the non-straight and straight boundaries ($u_{rms,ns}$ / $u_{rms,s}$) is approximately 1, indicating that the boundary geometry has little influence on the overall flow intensity. Second, in the transitional regime ($Ra = 1000$), $u_{rms,ns}$ / $u_{rms,s}$ increases to 1.68, suggesting that the non-straight boundary enhances convective motion, which is consistent with the maximum Nu/Ra enhancement of 2.43 shown in Fig. 3(b). Third, in the high-Rayleigh-number regime ($Ra > 1000$), $u_{rms,ns}$ / $u_{rms,s}$ decreases below unity. For example, $u_{rms,ns}$ / $u_{rms,s}$ is 0.66 at $Ra = 300\,000$, indicating that the non-straight boundary suppresses the overall flow intensity. This velocity suppression is consistent with the reduction in heat transfer discussed

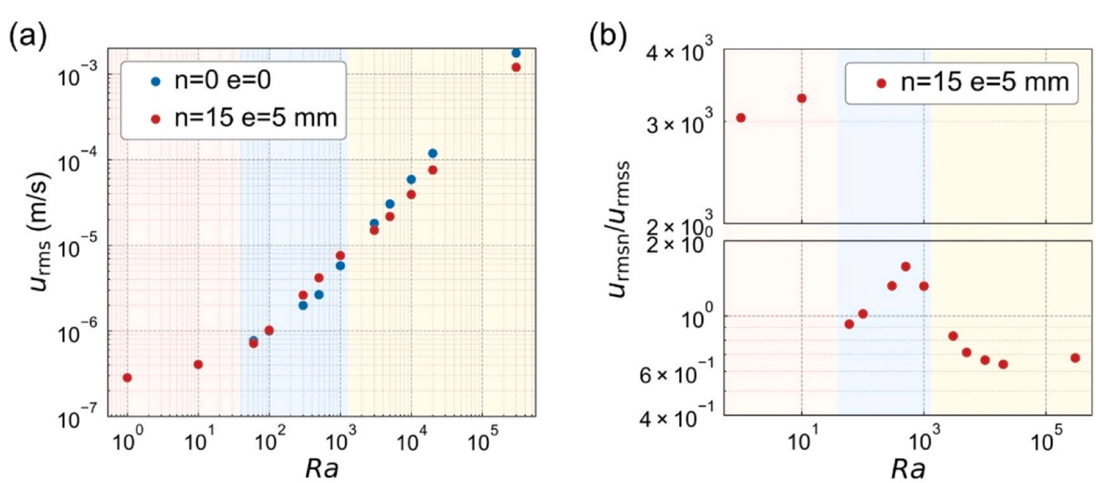

Fig. 5. Root-mean-square velocity u_{rms} at statistical steady state for the representative non-straight boundary ($n = 15$, $e = 5$ mm). Here u_{rms} denotes the domain-averaged temporal root-mean-square of the Darcy-velocity magnitude over the statistically steady averaging window. (a) u_{rms} for straight and non-straight boundaries. (b) Ratio $u_{rms,ns}$ / $u_{rms,s}$. The $n = 15$, $e = 5$ mm case is selected here because it provides the clearest enhancement-to-suppression crossover in the full dataset; results for the other non-straight geometries, including $n = 30$, are provided in Supplementary Material Section S5.

above.

From a physical standpoint, this indicates that in regime I the non-straight bottom boundary induces local convection that makes a positive contribution to global convective transport, as is clearly visible in Fig. 4. In regime II, the local convection generated in the non-straight-bottom configuration is broadly aligned with the global convection pattern and therefore does not provide a clearly positive or negative additional contribution. In regime III, however, the local convection associated with the non-straight bottom boundary is no longer aligned with the global convection, and it exerts a negative influence on the overall convective transport.

From Fig. 2(c), it can be observed that for $Ra = 1$, during the

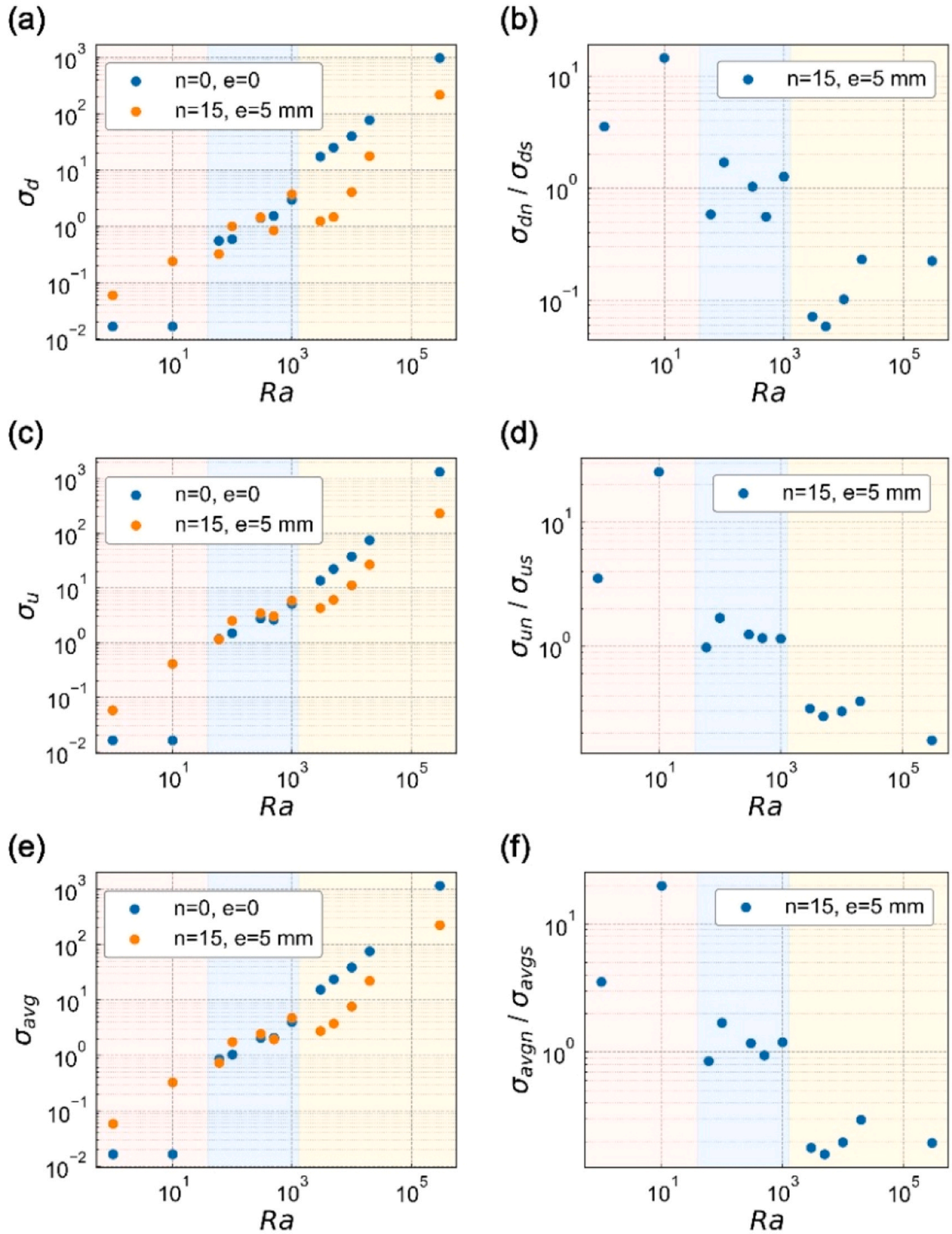

Fig. 6. Standard deviation of the boundary heat flux during the statistical steady state. (a) Lower-boundary heat-flux standard deviation for straight and non-straight bottom configurations. (b) Ratio of the lower-boundary heat-flux standard deviation for the non-straight configuration to that for the straight configuration. (c) Upper-boundary heat-flux standard deviation for straight and non-straight bottom configurations. (d) Ratio of the upper-boundary heat-flux standard deviation for the non-straight configuration to that for the straight configuration. (e) Mean value of the upper- and lower-boundary heat-flux standard deviations for straight and non-straight bottom configurations. (f) Ratio of this mean value for the non-straight configuration to that for the straight configuration. The $n = 15$, $e = 5$ mm case is selected here because it provides the clearest enhancement-to-suppression crossover in the full dataset; results for the other non-straight geometries, including $n = 30$, are provided in Supplementary Material Section S5.

statistical steady state the heat flux at both the upper and lower boundaries varies very slowly and smoothly. This is consistent with existing theory, according to which transport is primarily diffusion-controlled and no convection occurs at this stage. In contrast, for $Ra = 3000$, once the system reaches the statistical steady state, the heat fluxes at both boundaries exhibit strong oscillations, and the steady state is attained much more rapidly. Therefore, Fig. 2 supports the view that heat transfer is convection-dominated at high Ra. However, Fig. 2 also reveals another important feature: at high Rayleigh numbers, during the statistical steady state, fluctuations in the dimensionless heat flux are smaller for the non-straight bottom boundary, indicating that convection is more stable under the non-straight bottom boundary than under the straight bottom boundary. To verify this conclusion over a broader range of Ra, we further analyze the upper and lower boundary heat fluxes for both straight and non-straight bottom boundaries at different Rayleigh numbers.

Fig. 6 shows the standard deviation of the heat flux in the statistical steady state as a function of Ra. From Fig. 6(a), 6(c), and 6(e), three regimes can be identified. In Regime I, the standard deviation of the steady-state heat flux for the non-straight bottom boundary is significantly larger than that for the straight boundary, whose standard deviation is nearly zero. This is because heat transfer remains diffusion-dominated for the straight boundary at low Ra, so the heat flux exhibits almost no temporal fluctuation in the steady state. In Regime II, the standard deviations for the straight and non-straight bottom boundaries become comparable. In Regime III, the standard deviation for the straight boundary is clearly larger than that for the non-straight bottom boundary, confirming that convection is more stable under the non-straight geometry. The same trends are also evident in Fig. 6(b), 6(d), and 6(f), which show the ratio of the standard deviation of the heat flux in the statistical steady state for the non-straight configuration to that for the straight configuration. In Regime I, this ratio is much greater than one; in Regime II, it is approximately equal to one; and in Regime III, it decreases to values below one. These behaviors are consistent with the heat-flux fluctuation trends shown in Fig. 6(a), 6(c), and 6(e).

Fig. 7(a) presents the density distribution for the straight-boundary case after the system has reached a statistically steady state and the fields have been averaged in time. Here, the dimensionless height is $y = y/h$, and the horizontally averaged dimensionless density denotes the average of the dimensionless density along the horizontal direction at a given y.

$$\bar{\rho} = \langle\tilde{\rho}\rangle_{\bar{y}}.$$

Fig. 7(a) illustrates how the flow behavior evolves under the influence of density gradients as Ra increases. The density profiles progressively shift rightward and become steeper, indicating stronger thermally driven buoyancy convection and a more pronounced nonlinear response of the system. When $Ra < 4\pi^2$ (Regime I), the density varies almost linearly with height, indicating diffusion-dominated transport. When $4\pi^2 < Ra < 1300$ (Regime II), the density near the lower boundary initially increases rapidly with height, then rises more gradually in the middle region, and again increases sharply near the upper boundary. Distinct boundary layers form at both the upper and lower interfaces. When $Ra > 1300$ (Regime III), the density profile exhibits strong vertical variations with pronounced boundary layers at both the top and bottom. These boundary layers are thinner than those observed at moderate Ra.

From Fig. 7(b), distinct behaviors are observed as the Rayleigh-Darcy number increases. In the present paper, Ra around 1300 is retained as a reference threshold from previous straight-boundary studies of Nu/Ra, where it mark$_s$ the transition into the high-Ra regime. For the non-straight configuration studied here, the density profiles show that the same interval also corresponds to the point at which trough convection ceases to remain fully connected to the bulk circulation. When $Ra < 1300$ (Regimes I and II), a clear density inversion persists between the crest ($y = 0.25$) and the trough ($y = -0.25$), being higher near the top and lower near the bottom. This unstable stratification triggers active convection within the troughs, integrates this region into the global circulation, and enhances heat transfer. As a result, over the entire domain (from $y = -0.25$ to $y = 1$), the effective heat-transfer height approaches $h + e$, which is greater than h, leading to a higher convective efficiency Nu/Ra than in the straight-boundary case. In contrast, when $Ra > 1300$ (Regime III), the fluid within the troughs becomes strongly stratified and nearly vertically uniform in density, effectively forming stagnant dead zones that do not contribute to the overall convective transport. Consequently, the active convective region is lifted above the troughs, reducing the effective heat-transfer height to approximately $h - e$. In this sense, the adopted classical threshold remains a useful organizing reference, while its physical manifestation in the present geometry is the onset of trough stagnation and the associated reduction of the effective convective height.

This mechanism is visually corroborated by the instantaneous density and flow-field visualizations. For example, in the density evolution shown in Fig. 2(b) for $Ra = 100$ and $Ra = 1000$, a strong density contrast is maintained even deep within the regions between the crest and trough. Similarly, the flow field for $Ra = 500$ in Fig. 4(f) confirms the presence of active convective rolls extending into these regions, contributing to the overall heat transfer. The effective transfer height therefore approaches $h + e$, explaining the enhanced efficiency. By contrast, at higher Rayleigh numbers ($Ra = 3000$, 20 000, and 300 000) in Fig. 2(b), the density in the troughs becomes progressively more homogenized. The case $Ra = 20\,000$ is used as a representative Regime III field-visualization case because it shows a clearly developed high-Ra structure and pronounced heat-transfer suppression, whereas $Ra = 300\,000$ represents the highest simulated Rayleigh-Darcy number. As seen in the flow field for $Ra = 10\,000$ in Fig. 4(h), the main convective flow bypasses the troughs, creating a thermal short-circuit. At $Ra = 300\,000$, this bypassing tendency persists and the troughs behave as nearly stagnant pockets. Hence, the stagnant fluid in the troughs does not

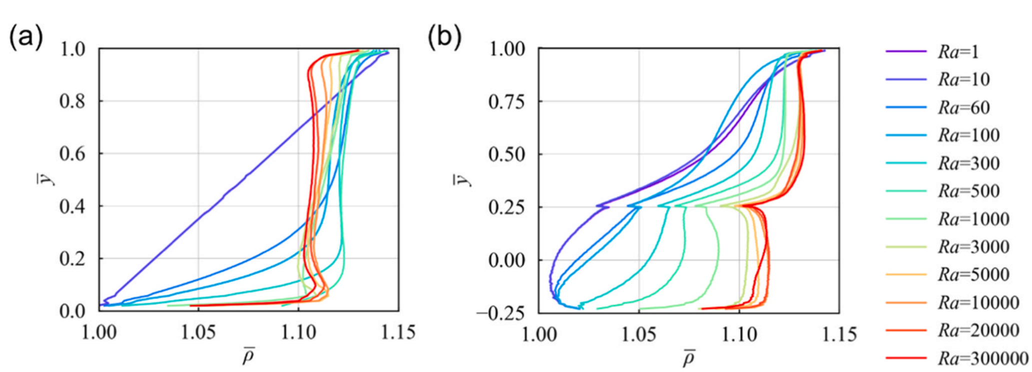

Fig. 7. Horizontally averaged density profiles at statistical steady state for (a) the straight boundary and (b) the representative non-straight boundary ($n = 15$, $e = 5$ mm).

contribute to the overall heat transfer. The effective transfer height then approaches $h - e$, which is smaller than h, resulting in a lower Nu/Ra than that of the straight boundary in Fig. 3.

3.4. Heat transfer characteristics

Extensive research has been conducted at high Ra, leading to the development of the Grossmann-Lohse (GL) theory [26]. The central idea of the GL theory is to decompose the total thermal and kinetic energy dissipation rates into separate contributions from the boundary layer (BL) and the bulk flow region. This decomposition enables a clearer assessment of how the boundary layers and the bulk flow individually influence the overall heat transfer and dynamical behavior of a convective system. The variations of the horizontally averaged dimensionless density with dimensionless height at high Ra in Fig. 7 are consistent with the trends predicted by the GL theory.

Fig. 8(a) shows the spatial distribution of convective thermal dissipation under statistically steady conditions for the straight boundary. At high Ra, the dissipation is primarily concentrated in thin thermal boundary layers near the upper and lower boundaries, while the contribution from the bulk region is negligible. This indicates that global heat transport is primarily controlled by boundary-layer processes, and the main scaling behavior of the Nusselt number Nu with Ra can be inferred from the dynamics of these boundary layers. This feature is consistent with previous studies [10], which showed that, for high Rayleigh numbers, the boundary layers, rather than the well-mixed bulk, provide the dominant contribution to thermal dissipation and therefore determine the heat-transfer scaling.

Fig. 8(b) presents the convective thermal dissipation field under statistically steady conditions for the non-straight-bottom configuration. In this case, the dissipation pattern differs markedly from that of the straight-bottom case. While the thermal dissipation remains concentrated in the upper boundary layer, it is also strongly enhanced along the entire non-straight bottom boundary, including both the crests and troughs. This indicates that the undulations of the boundary significantly intensify local gradients and promote vigorous small-scale convection near the bottom. As a result, the effective contribution of the lower boundary region, which extends over the entire undulating non-straight bottom boundary rather than being confined to a thin boundary layer, to the total thermal dissipation is substantially enhanced. This highlights the crucial role of the non-straight interface geometry in modulating global heat-transfer characteristics.

Fig. S3 shows numerous convective fingers during the convection process. These fingers increase the effective heat-transfer area and therefore tend to enhance the overall transfer efficiency. Thus, the number of convective fingers, f, provides a useful indicator of convective activity, although it is not the sole determinant of Nu/Ra. The steady-state values of f are statistically summarized in Fig. 9: (1) When $Ra < 1000$, the convective finger number f for the non-straight bottom boundary is greater than that for the straight bottom boundary, indicating that the non-straight configuration generates additional convective fingers and thereby strengthens convection. (2) However, when $Ra > 1000$, the non-straight bottom boundary suppresses the convective finger number f compared with the straight bottom boundary.

It is noteworthy that the threshold Ra around 1000, where the non-straight boundary begins to yield fewer fingers than the straight boundary, precedes the classical heat-transfer regime boundary near Ra around 1300 adopted in Fig. 3. The latter value is retained as a reference from previous straight-boundary studies of Nu/Ra, whereas the finger-number threshold is determined directly from the present simulations. The offset therefore indicates that finger reduction begins earlier than the actual efficiency crossover.

In the intermediate interval $1000 < Ra < 1300$, the non-straight geometry already suppresses finger generation relative to the straight boundary, but the trough region is still dynamically connected to the main circulation, so the effective convective height remains closer to $h + e$ than to h − e. The geometric gain therefore compensates for the reduced finger number, and Nu/Ra stays above the straight-boundary value. Only after Ra exceeds about 1300 do both effects act in the same direction: finger suppression persists and trough stratification establishes stagnant pockets, lifting the active circulation above the troughs. At that point the effective height decreases toward $h - e$, and the non-straight configuration crosses over to lower Nu/Ra.

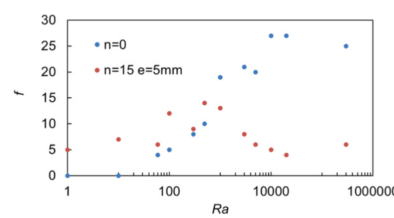

Fig. 9. Number of convective fingers at different Ra. The blue dots represent the convective finger number f for the straight bottom boundary, while the red dots represent f for the non-straight bottom boundary. The convective finger number f is defined as the number of sign changes in the vertical velocity along the line at $x = L/2$. The reduction in f for the non-straight boundary begins near Ra around 1000, earlier than the efficiency crossover near Ra around 1300, because the latter still follows the classical Nu/Ra-based regime reference, whereas the finger-number threshold is identified directly from the present simulations; see the discussion below in this section.

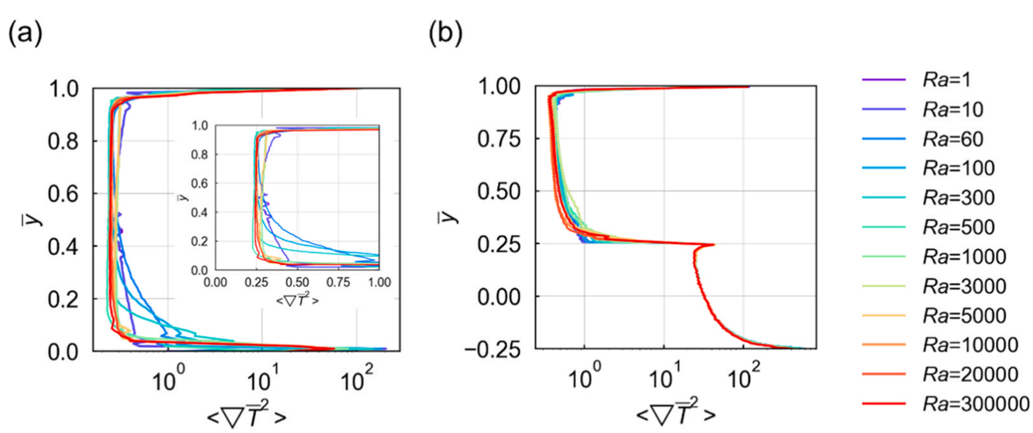

Fig. 8. Horizontal- and time-averaged dimensionless thermal dissipation at statistical steady state for (a) the straight boundary and (b) the representative non-straight boundary ($n = 15$, $e = 5$ mm).

4. Conclusion

This study addresses one central question: how a sinusoidal non-straight bottom boundary changes heat-transfer efficiency relative to the classical straight-boundary case as the Rayleigh-Darcy number increases. High-resolution simulations reveal a regime-dependent crossover in Nu/Ra and identify the stagnant-trough-induced thermal-short-circuit mechanism that controls this transition. The main conclusions are drawn as follows:

(1) Three distinct heat transfer regimes are identified based on the variation of Nu/Ra. In Regime I ($Ra < 4\pi^2$) and Regime II ($4\pi^2 < Ra < 1300$), the non-straight boundary significantly enhances heat transfer efficiency compared to the straight boundary, with a maximum enhancement factor of 2.43 observed in the diffusion-dominated limit. In contrast, in Regime III ($Ra > 1300$), the non-straight boundary suppresses heat transfer, resulting in a reduction of efficiency by ~32% at $Ra = 3 \times 10^5$ compared to the straight configuration.

(2) The crossover behavior is governed by a competition between geometric enhancement and flow stratification. In lower Ra regimes, the troughs of the non-straight boundary induce localized convection, increasing the effective convective height to approximately $h + \mathrm{e}$. However, in the high-Ra regime (Regime III), the fluid within the troughs becomes stagnant and stratified, forming "dead zones" that decouple from the bulk circulation. This creates a "thermal short-circuit" where the active convection bypasses the troughs, reducing the effective convective height to $h - e$ and consequently degrading the overall heat transfer.

(3) The proposed mechanism is supported by scaling analysis and field diagnostics. The heat transfer scaling in the straight-boundary configuration aligns well with the classical Grossmann-Lohse (GL) theory predictions and previous benchmark$_s$. Importantly, the deviation of the scaling exponent in the non-straight configuration at high Ra quantitatively supports the suppression effect of the stagnant zones.

The supplementary parameter comparisons show that the strength and onset of this boundary-induced regulation depend on wavenumber and amplitude, while the representative $n = 15$, $e = 5$ mm case captures the clearest enhancement-to-suppression crossover. This study provides insight into how natural and engineered non-straight boundaries may regulate convective heat transfer in porous media, with implications for geothermal reservoirs, permafrost thawing, and subsurface energy systems.

CRediT authorship contribution statement

Ke Xu: Writing – review & editing, Supervision, Project administration, Methodology, Funding acquisition, Conceptualization. **Jiansong Wu:** Writing – review & editing, Supervision, Resources, Project administration, Funding acquisition. **Yumin Wang:** Writing – review & editing, Writing – original draft, Visualization, Validation, Software, Methodology, Investigation, Formal analysis, Data curation, Conceptualization.

Funding

We gratefully acknowledge the financial support and funding provided by National Key Research and Development Program of China under Grant No. 2023FYA1011701, National Key Research and Development Program of China under Grant No. 2023YFC3011300, China Postdoctoral Science Foundation under Grant No. 2025M781758, and the China National Petroleum Corporation-Peking University Strategic Cooperation Project of Fundamental Research.

Declaration of Competing Interest

We declare no conflict of interest.

Acknowledgments

N\a.

Appendix A. Supporting information

Supplementary data associated with this article can be found in the online version at doi:10.1016/j.ijheatmasstransfer.2026.129024.

Data availability

All data needed to evaluate the conclusions in the paper are present in the paper and/or the Supplementary Materials.

References

[1] D.R. Hewitt, Vigorous convection in porous media, Proc. R. Soc. A. 476 (2020) 20200111, https://doi.org/10.1098/rspa.2020.0111.
[2] M. De Paoli, Convective mixing in porous media: a review of Darcy, pore-scale and H ele-Shaw studies, Eur. Phys. J. E 46 (2023) 129, https://doi.org/10.1140/epje/s10189-023-00390-8.
[3] D.A. Nield, A. Bejan, Convection in porous media, Springer New York, New York, NY, 2013, https://doi.org/10.1007/978-1-4614-5541-7.
[4] W. Xue, Y. Wang, Z. Chen, H. Liu, An integrated model with stable numerical methods for fractured underground gas storage, J. Clean. Prod. 393 (2023) 136268, https://doi.org/10.1016/j.jclepro.2023.136268.
[5] C.W. Horton, F.T. Rogers, Convection currents in a porous medium, J. Appl. Phys. 16 (1945) 367–370, https://doi.org/10.1063/1.1707601.
[6] E.R. Lapwood, Convection of a fluid in a porous medium, Math. Proc. Camb. Philos. Soc. 44 (1948) 508–521, https://doi.org/10.1017/S030500410002452X.
[7] N.R. Sgreva, C. Metivier, A. Teixeira, T.D. Le, S. Leclerc, Experimental velocity and temperature measurements for natural convection in a highly porous medium, Int. J. Therm. Sci. 205 (2024) 109257, https://doi.org/10.1016/j.ijthermalsci.2024.109257.
[8] D.J. Keene, R.J. Goldstein, Thermal convection in porous media at high Rayleigh numbers, J. Heat. Transf. 137 (2015), https://doi.org/10.1115/1.4029087.
[9] J.W. Elder, Steady free convection in a porous medium heated from below, J. Fluid Mech. 27 (1967) 29–48, https://doi.org/10.1017/S0022112067000023.
[10] X. Zhu, Y. Fu, M. De Paoli, Transport scaling in porous media convection, J. Fluid Mech. 991 (2024) A4, https://doi.org/10.1017/jfm.2024.528.
[11] S. Pirozzoli, M. De Paoli, F. Zonta, A. Soldati, Towards the ultimate regime in Rayleigh–Darcy convection, J. Fluid Mech. 911 (2021) R4, https://doi.org/10.1017/jfm.2020.1178.
[12] A. Paolillo, F. Colella, N. Nosengo, F. Schiano, W. Stewart, D. Zambrano, I. Chappuis, R. Lalive, D. Floreano, How to compete with robots by assessing job automation risks and resilient alternatives, Sci. Robot 7 (2022) eabg5561, https://doi.org/10.1126/scirobotics.abg5561.
[13] J. Li, Y. Yang, C. Sun, From Darcy convection to free-fluid convection: pore-scale study of density-driven currents in porous media, J. Fluid Mech. 1009 (2025) A10, https://doi.org/10.1017/jfm.2025.213.
[14] Z.-H. Xuan, W.-Z. Fang, Y.-H. Lu, C. Yang, W.-Q. Tao, Significance of the natural convection to the heat transfer of porous media: A pore-scale study, Int. J. Heat. Mass Transf. 222 (2024) 125163, https://doi.org/10.1016/j.ijheatmasstransfer.2023.125163.
[15] S. Gasow, A.V. Kuznetsov, Y. Jin, Prediction of pore-scale-property dependent natural convection in porous media at high Rayleigh numbers, Int. J. Therm. Sci. 179 (2022) 107635, https://doi.org/10.1016/j.ijthermalsci.2022.107635.
[16] P.G. Siddheshwar, M. Narayana, D. Laroze, C. Kanchana, Brinkman–Bénard convection with rough boundaries and third-type thermal boundary conditions, Symmetry 15 (2023) 1506, https://doi.org/10.3390/sym15081506.
[17] X. Tian, Z. Ye, Experimental study on convection heat transfer properties in rough-walled fractures of granite: the effect of fracture roughness, Geothermics 122 (2024) 103085, https://doi.org/10.1016/j.geothermics.2024.103085.
[18] M.M. Rahman, M.Z. Saghir, K. Vajravelu, I. Pop, Free convective heat transfer flow in a glass bead porous medium varying permeability and sinusoidal wall temperature, J. Therm. Anal. Calorim. 150 (2025) 551–572, https://doi.org/10.1007/s10973-024-13535-4.
[19] S.D. Hwang, I.H. Jang, H.H. Cho, Experimental study on flow and local heat/mass transfer characteristics inside corrugated duct, Int. J. Heat. Fluid Flow. 27 (2006) 21–32, https://doi.org/10.1016/j.ijheatfluidflow.2005.07.001.
[20] H.G. Kwon, S.D. Hwang, H.H. Cho, Flow and heat/mass transfer in a wavy duct with various corrugation angles in two dimensional flow regimes, Heat. Mass Transf. 45 (2008) 157–165, https://doi.org/10.1007/s00231-008-0422-4.
[21] Y. Wang, J.-H. Xie, W. Yang, X. Li, Z. Abulaiti, S. Zheng, J. Zhu, K. Xu, Permafrost thawing under overlaying salt water, Sci. Adv. 11 (2025) eadp2808, https://doi.org/10.1126/sciadv.adp2808.

[22] L. Durlofsky, J.F. Brady, Analysis of the Brinkman equation as a model for flow in porous media, Phys. Fluids 30 (1987) 3329–3341, https://doi.org/10.1063/1.866465.

[23] J. Bear, Dynamics of Fluids in Porous Media. Reprint. Originally published: New York: American Elsevier. Pub. Co., 1972. Originally published in series: Environmental science series (New York, 1972-). With corrections, Dover Publ, New York, 2013.

[24] D.R. Hewitt, J.A. Neufeld, J.R. Lister, Ultimate regime of high rayleigh number convection in a porous medium, Phys. Rev. Lett. 108 (2012) 224503, https://doi.org/10.1103/PhysRevLett.108.224503.

[25] P.G. Saffman, G. Taylor, The penetration of a fluid into a porous medium or Hele-Shaw cell containing a more viscous liquid, in: P. Pelcé (Ed.), Dynamics of Curved Fronts, Academic Press, San Diego, 1988, pp. 155–174, https://doi.org/10.1016/B978-0-08-092523-3.50017-4.

[26] S. Grossmann, D. Lohse, Scaling in thermal convection: a unifying theory, J. Fluid Mech. 407 (2000) 27–56, https://doi.org/10.1017/S0022112099007545.